computer programs

PITRE: software for phase-sensitive X-ray image processing and tomography reconstruction

Rong-Chang Chen,[a]* Diego Dreossi,[b] Lucia Mancini,[b] Ralf Menk,[b] Luigi Rigon,[a] Ti-Qiao Xiao[c] and Renata Longo[a,d]

[a]INFN, Sezione di Trieste, Trieste, Italy, [b]Sincrotrone Trieste SCpA, Trieste, Italy, [c]Shanghai Institute of Applied Physics, Chinese Academy of Science, Shanghai, People's Republic of China, and [d]Dipartimento di Fisica, Università di Trieste, Trieste, Italy. E-mail: rongchang.chen@ts.infn.it

Synchrotron-radiation computed tomography has been applied in many research fields. Here, PITRE (Phase-sensitive X-ray Image processing and Tomography REconstruction) and PITRE_BM (PITRE Batch Manager) are presented. PITRE supports phase retrieval for propagation-based phase-contrast imaging/tomography (PPCI/PPCT), extracts apparent absorption, refractive and scattering information of diffraction enhanced imaging (DEI), and allows parallel-beam tomography reconstruction for conventional absorption CT data and for PPCT phase retrieved and DEI-CT extracted information. PITRE_BM is a batch processing manager for PITRE: it executes a series of tasks, created via PITRE, without manual intervention. Both PITRE and PITRE_BM are coded in Interactive Data Language (IDL), and have a user-friendly graphical user interface. They are freeware and can run on Microsoft Windows systems via IDL Virtual Machine, which can be downloaded for free and does not require a license. The data-processing principle and some examples of application will be presented.

Keywords: phase image; tomography reconstruction; image processing.

1. Introduction

X-ray computed tomography (CT) is a non-destructive technique widely used for visualizing the morphology of samples, and for assessing quantitative information on their three-dimensional (3D) geometries and properties (Kak & Slaney, 2001). CT has several advantages over traditional two-dimensional radiography. For instance, CT eliminates the superimposition of sample structures as apparent in radiographic images. The 3D structure of samples can be obtained for modelling and quantitative analysis (Brun et al., 2010). With the availability of third-generation synchrotron radiation (SR) sources, SR-CT has evolved as an increasingly accepted and utilized technique for characterizing the 3D internal structure of samples in the fields of material science and life sciences (biological and medical applications). SR-CT has many advantages compared with CT based on X-ray tube sources. Firstly, the monochromatic beam yields reconstructed CT images free of beam hardening artifacts and allows image calibration in order to evaluate the distribution of the linear attenuation coefficient of samples (Pani et al., 2004; Chen et al., 2010). Secondly, owing to the limited divergence of SR beams, the spatial resolution of SR-CT is limited mainly by the detector. Thirdly, rapid CT data acquisition with high spatial resolution is feasible with the high flux available at SR beams (Fife et al., 2012). Eventually, the high degree of (transverse) coherence of the SR beams allows implementation of phase-sensitive imaging techniques (Cloetens et al., 1996).

X-ray phase-sensitive imaging utilizes phase shifts rather than absorption information, which is employed in X-ray absorption imaging/CT, as the imaging signal. This substantially extends the possibilities of X-ray absorption imaging, especially when imaging low-Z samples (Snigirev et al., 1995; Wilkins et al., 1996) or when the difference in attenuation coefficient between different regions in the sample is too small to be detected (Cloetens et al., 1997). Several phase-sensitive imaging techniques have been developed, such as interferometric methods, analyser-based methods, grating-based methods, coded-aperture-based methods and propagation-based methods (Fitzgerald, 2000; Momose, 2005). All these methods have been successfully extended to CT mode (Bonse, 2008). Although X-ray imaging detectors are sensitive to intensity modulations only, the phase information is embedded in the recorded images too; however, this information cannot be accessed directly without any further processing. For instance, propagation-based phase-contrast imaging (PPCI) yields edge-enhancement information, which is proportional to the Laplacian of the refractive index distribution of the sample. It requires the so-called phase-retrieval processing to extract phase information (Nugent et al., 1996; Cloetens et al., 1999). Other phase-sensitive imaging methods also require their post-processing procedures, such as the extraction of apparent absorption, refraction and scattering information in diffraction enhanced imaging (DEI) (Chapman et al., 1997; Rigon et al., 2007a,b; Chou et al., 2007). Generally speaking, 3D information can then be obtained by applying standard filtered back-projection (FBP) CT reconstruction algorithms to the post-processed phase-sensitive projections (Cloetens et al., 1999; Dilmanian et al., 2000; Rigon et al., 2008).

Recent progress in detector development tends to decrease the pixel size while increasing the pixel number. As a consequence, a

large number of SR-CT projections (of the order of 1000) are required for existing CT algorithms to generate reconstructions without significant artifacts. Subsequently the amount of CT data has increased accordingly, sometimes exceeding several gigabytes. Therefore, tomographic data processing is a heavy computing task and a critical issue in CT experiments.

Almost ten years ago, at the SYRMEP (SYnchrotron Radiation for MEdical Physics) beamline (Abrami *et al.*, 2004) of the Elettra synchrotron facility (Trieste, Italy), the SYRMEP TOMO Project (STP) (Montanari *et al.*, 2003) was developed as a tool to address the needs of the rapidly increasing CT activities at the beamline. STP was used for SR-CT data processing supporting parallel CT reconstruction and had a user-friendly graphical user interface (GUI). STP was coded *via* Interactive Data Language (IDL) (IDL, 2012); the choice of IDL was because it allowed us to distribute STP to the beamline users, who could use it *via* the IDL Virtual Machine that can be downloaded for free and does not require a license.

Nowadays, phase-sensitive imaging techniques are widespread in SR-CT experiments. Besides qualitative reconstructions, which are obtained by applying the FBP to the phase-sensitive projections, quantitative reconstructions are also desired. These require post-processing of the phase-sensitive projections and corresponding 3D information reconstruction methods. Software packages which cover these interests have been presented by different research groups. For instance, the *ANKAphase* (Weitkamp *et al.*, 2011) processes PPCI radiographs by reconstructing the projected thickness of the object(s) image by utilizing a single-distance non-iterative phase-retrieval algorithm proposed by Paganin *et al.* (2002); but it does not perform tomographic reconstruction. *ANKAphase* is a free software and can be run as a plug-in to *ImageJ* (ImageJ, 2012), a widely used scientific image-processing program, or as a stand-alone application. Another choice is *X-TRACT* (Gureyev *et al.*, 2011), which is a software tool for X-ray image processing, analysis, reconstruction and simulation. It includes parallel codes that can run on multiple CPUs and GPUs. Detailed information about the software and its capabilities can be found on its website (X-TRACT, 2012), where one can also open an on-line account and subsequently download a fully functional version of *X-TRACT* for a time-limited trial (Gureyev *et al.*, 2011). Other possibilities are some in-house software, such as the holotomography processing program at ESRF (Cloetens *et al.*, 1999; Holotomography, 2012) and tomography processing software at the TOMCAT beamline of the Swiss Light Source (Hintermüller *et al.*, 2010).

Inspired by the above-mentioned software and considering the specific needs of the experiments at the SYRMEP beamline at Elettra and the BL13W1 beamline at SSRF, we have developed a software package that supports phase retrieval for propagation-based phase-contrast imaging/tomography (PPCI/PPCT), extracting apparent absorption, refractive and scattering information from DEI, and tomographic reconstruction for conventional absorption CT data and for PPCT phase retrieved and DEI-CT extracted information. It also provides specific features to elaborate data acquired by the PICASSO (Phase Imaging for Clinical Applications with Silicon detector and Synchrotron radiatiOn) prototype, which is a silicon edge-on micro-strip detector developed by Istituto Nazionale di Fisica Nucleare and installed at the SYRMEP beamline (Rigon *et al.*, 2010a; Lopez *et al.*, 2011). The software, which is written in IDL, comprises *PITRE* (Phase-sensitive X-ray Image processing and Tomography REconstruction, version 3) and *PITRE_BM* (*PITRE* Batch Manager), which runs on top of *PITRE* in batch processing mode. The acronym *PITRE* in Italian is pronounced /'pi.tre/; the pronunciation is the same as 'P3', which is chosen as a logo for the *PITRE* program.

The data-processing principle and some examples of application will be herein provided.

2. Methods

Since its first release in late-2008, *PITRE* has been available at the BL13W1 beamline at SSRF and the SYRMEP beamline at Elettra for processing SR-CT data (Lu *et al.*, 2010; Liu *et al.*, 2010; Chen *et al.*, 2010, 2011a,b; Rigon *et al.*, 2010b, 2011; Tang *et al.*, 2011; Deng *et al.*, 2011; Zhang *et al.*, 2011; Hu *et al.*, 2012; Yang *et al.*, 2012; Sodini *et al.*, 2012). These studies cover both qualitative and quantitative investigation, such as 3D neurovascular morphology investigation of rat spinal cord (Hu *et al.*, 2012), line attenuation coefficient measurement of breast tissues (Chen *et al.*, 2010) and 3D distribution of the real part of the refractive index reconstruction (Chen *et al.*, 2011a,b). The data-processing flow of *PITRE* is shown in Fig. 1, in which the red, blue and green boxes represent input data, processing functions and output data, respectively. The arrows denote the data flow direction. In *PITRE*, the output data can also be input for further processing: for instance, the phase-retrieval result can be input for the sinogram generation. In this section the *PITRE* data-processing principle will be presented. It includes flat-field and dark-field correction, PPCT phase retrieval, DEI extraction, sinogram generation and pre-processing, and slice reconstruction.

2.1. Flat-field and dark-field correction

In the practical case of a SR-CT experiment, the monochromator may introduce background features into the illuminating beam. The scintillator and the optical components of the image receptor may not be perfect as well. Moreover, the beryllium windows and filters can introduce artifacts if they are not properly polished. All these features affect the intensity profile recorded by the detector. In order to avoid artifacts in the reconstructed image, these intensity modulations have to be corrected. The associated procedure is referred to as flat-field correction. Moreover, each image recorded with the detector possesses an offset signal (dark signal in the absence of
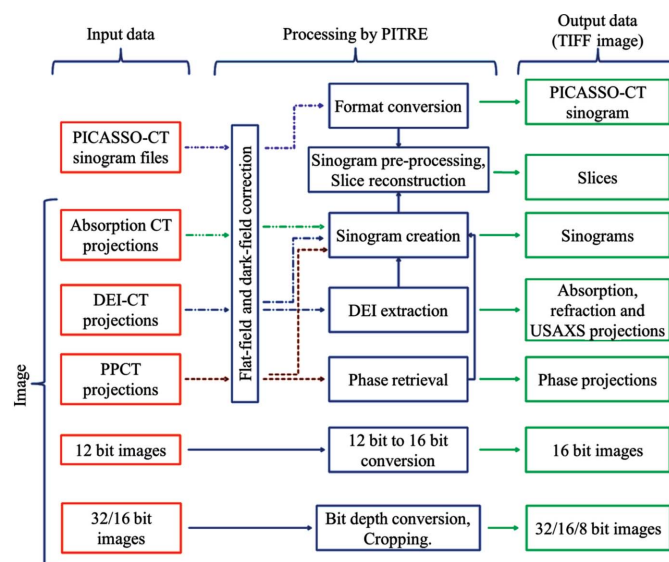
Figure 1
PITRE data processing flow. The red, blue and green boxes represent input data, *PITRE* processing functions and output data, respectively, and the arrows denote the data flow direction.

photons) that has to be subtracted from the image before further processing (dark-field correction). The corrected projection I_{PC} is

$$I_{PC} = \frac{I_P - I_D}{I_F - I_D}, \tag{1}$$

where I_P, I_F and I_D are the recorded projection, flat-field and dark-field image, respectively. During this procedure the dark-current subtraction ($I_P - I_D$ and $I_F - I_D$) may create zeros or even negative values; this is problematic when performing the natural logarithm during the reconstruction, and thus corrupts the result. In *PITRE*, these zeros or even negative values in $I_P - I_D$ and $I_F - I_D$, if they occur, will be replaced by $\mathrm{mean}(I_P - I_D)/1000$ and $\mathrm{mean}(I_F - I_D)/1000$, respectively, where $\mathrm{mean}(\ldots)$ represents the mean value. In this case this problem will be corrected and the substitute value is small so it does not affect the quantitative nature of the reconstruction.

2.2. Phase retrieval for propagation-based phase-contrast tomography

PPCT has widely attracted attention owing to its particularly simple experimental set-up, which is identical to absorption-based CT except for its increased sample-to-detector distance (SDD) (Cloetens *et al.*, 1996) provided that the SR beam is sufficient spatially coherent. Phase retrieval is a technique for obtaining phase information from PPCT radiography fringes (Nugent *et al.*, 1996; Cloetens *et al.*, 1999). In general, phase retrieval requires at least two measurements of the intensity, taken at two different SDDs. In PPCT, hundreds or thousands of projections will be taken. Taking PPCT data at two different SDDs will increase the experiment time and deliver a higher radiation dose to the sample, which could hinder its biomedical applications. Definitely, phase retrieval utilizing only single SDD PPCT data is preferable and more feasible, especially when dose is an essential issue in the experiment. Compared with multi-SDDs PPCT phase-retrieval algorithms, single-SDD ones require that the sample fulfils additional conditions, such as weak absorption and phase-attenuation duality (PAD) (Paganin *et al.*, 2002; Wu *et al.*, 2005). If the investigated sample does not fulfil these conditions, the quantitative result will not be preserved although quantitatively reasonable results may still be obtained.

In the following the principle of two phase-retrieval algorithms, which are implemented in *PITRE*, will be shown. They are called the phase-attenuation-duality Born algorithm (PAD-BA) and the phase-attenuation-duality modified Bronnikov algorithm (PAD-MBA). These two phase-retrieval algorithms are both based on the PAD property and employ only single SDD PPCT data.

Suppose that an object is illuminated by a monochromatic plane X-ray beam. Typically, the object can be described by its 3D complex refractive index distribution, $n(x, y, z) = 1 - \delta(x, y, z) + i\beta(x, y, z)$, where δ and β are the refractive index decrement and the absorption index, respectively, and (x, y, z) are the spatial coordinates. Because of the weak interaction of X-rays with matter, the beam propagation path inside the sample can be assumed to be a straight line and L denotes the linear path in the sample (Born & Wolf, 1999). The sample phase function $\varphi_\theta(x, y)$ and absorption function $\gamma_\theta(x, y)$ are, respectively,

$$\begin{aligned} \varphi_\theta(x, y) &= k \int_{L\theta} \delta(x, y, z) \, dz, \\ \gamma_\theta(x, y) &= k \int_{L\theta} \beta(x, y, z) \, dz, \end{aligned} \tag{2}$$

where $k = 2\pi/\lambda$ is the wavenumber, λ is the wavelength and $\int_{L\theta}$ denotes the line integral over the object along the beam path L at CT rotation angle θ.

When a sample is quasi-homogeneous, the real and imaginary parts of its complex refraction index are proportional to each other (PAD property) (Paganin *et al.*, 2002; Wu *et al.*, 2005),

$$\delta(x, y, z) = \varepsilon\beta(x, y, z), \tag{3}$$

where ε is a constant. The ε value depends on the particular sample. In both PAD-BA and PAD-MBA of *PITRE*, the user should manually provide this value, which can be obtained from X-ray databases such as CXRO (CXRO, 2012; Henke *et al.*, 1993).

2.2.1. Phase-attenuation duality Born algorithm. The PAD-BA was proposed by Gureyev *et al.* (2004) and is designed for low-Z and homogeneous materials. Later it was extended to tomography and applied to quasi-homogeneous objects (Chen *et al.*, 2011a). In the PAD-BA, the 3D refractive-index decrement reconstruction is based on a two-step approach: first, the phase function is retrieved for each PPCT projection by PAD-BA, and then the 3D distribution of the refractive-index decrement is reconstructed by applying the standard FBP algorithm.

Let us assume an object of weak absorption, $\gamma(x, y) \ll 1$, and slowly varying phase shift, *i.e.* obeying Guigay's condition $|\varphi(x + \lambda z\xi, y + \lambda z\eta) - \varphi(x, y)| \ll 1$ (Guigay, 1977), where (ξ, η) are the spatial frequencies in the Fourier space corresponding to a point (x, y) in real space, and z is the SDD. According to the Born-type approximation of the PPCI theory, the intensity distribution $I_{\theta, z}$ at SDD = z and rotation angle θ of PPCT can be approximated by the following equation (Gureyev *et al.*, 2004),

$$\mathcal{F}[(I_{\theta, z} / I_{\theta, 0} - 1)/2](\xi, \eta) = \hat{\gamma}_\theta \cos\chi + \hat{\varphi}_\theta \sin\chi, \tag{4}$$

where $\hat{\varphi}$ and $\hat{\gamma}$ denote the Fourier transform of the phase and the absorption function, φ and γ, respectively, and $\chi = \pi\lambda z(\xi^2 + \eta^2)$.

In the case where the PAD condition is fulfilled and for weakly absorbing samples, *i.e.* $I_{\theta, 0} \simeq 1$, substituting (3) into (4) yields the following equation (Gureyev *et al.*, 2004),

$$\varphi_\theta(x, y) = \mathcal{F}^{-1}\left\{ \frac{\mathcal{F}[(I_{z, \theta} - 1)/2]}{\varepsilon^{-1}\cos\chi + \sin\chi} \right\}. \tag{5}$$

Equation (5) retrieves the phase function of a phase-amplitude sample by using a single SDD PPCT projection.

After retrieving the phase function for the entire set of PPCT projections, the 3D refractive index can be reconstructed by applying the standard FBP algorithm to $\varphi_\theta(x, y)$ (Chen *et al.*, 2011a), that is

$$\delta(x, y, z) = k^{-1} \int_0^\pi \varphi_\theta(x, y) * \nu \, d\theta, \tag{6}$$

where $*$ denotes a one-dimensional convolution and ν is the CT reconstruction filter.

2.2.2. Phase-attenuation duality modified Bronnikov algorithm. In contrast to the two-step refractive index reconstruction approach, Bronnikov proposed an alternative theory that requires no intermediate step of phase retrieval and provides a direct reconstruction of the 3D refractive index from the PPCT projections (Bronnikov, 2002). This theory is based on a fundamental relation between the 3D Radon transform of the object function and the two-dimensional Radon transform of the PPCT projection. Later, Groso introduced an absorption correction factor (ACF; α) in the Bronnikov algorithm, naming it the modified Bronnikov algorithm (MBA). The MBA has been successfully applied to a phase-amplitude sample by using single SDD PPCT data (Groso *et al.*, 2006). The ACF has been further investigated by different groups on the basis of the PAD property of

low-Z samples (Gureyev *et al.*, 2006; Arhatari *et al.*, 2007; Chen *et al.*, 2011b).

When a monochromatic plane X-ray beam illuminates a sample, which is quasi-homogeneous and weakly absorbing, the intensity distribution $I_{\theta,z}$ at SDD = z and rotation angle θ is approximated according to the transport-of-intensity equation (Nugent *et al.*, 1996),

$$I_{\theta,z}(x,y) = I_{\theta,0}(x,y)\left[1 - \frac{\lambda z}{2\pi}\nabla^2\varphi_\theta(x,y)\right]. \qquad (7)$$

Reformulating (7) as $\nabla^2\varphi_\theta(x,y) = -(2\pi/\lambda z)g_\theta(x,y)$ with $g_\theta(x,y) = I_{\theta,z}/I_{\theta,0} - 1$, and applying the 2D and 3D Radon transform to $g_\theta(x,y)$ and $\delta(x,y,z)$, respectively, the 3D refractive index decrement $\delta(x,y,z)$ of the object can be reconstructed *via* the following equation that is the main result of the Bronnikov algorithm (Bronnikov, 2002),

$$\delta(x,y,z) = \frac{1}{4\pi^2 z}\int_0^\pi \left[q(x,y) ** g_\theta(x,y)\right]\,\mathrm{d}\theta, \qquad (8)$$

where $**$ indicates a two-dimensional convolution, and $q(x,y) = |y|/(x^2+y^2)$ is a filter. The Bronnikov algorithm is designed for pure phase objects (no absorption), such that it is unlikely to be fulfilled in practical cases. For a weakly absorbing sample ($I_{\theta,0} \simeq 1$), Groso introduced a modified $q(x,y)$ with an additional ACF; its Fourier space form is (Groso *et al.*, 2006)

$$Q(\xi,\eta) = \frac{|\xi|}{\xi^2 + \eta^2 + \alpha}, \qquad (9)$$

where α is the ACF, which is determined by using a semi-empirical (simulations and experiment) approach in MBA. However, considering the PAD property of the sample, an extremely simple ACF, $\alpha = 1/\pi\varepsilon\lambda z$, can be obtained (Gureyev *et al.*, 2006; Arhatari *et al.*, 2007; Chen *et al.*, 2011b). This ACF takes the energy, SDD and sample PAD property of the PPCT experiment into account. The PAD-MBA is the combination of (8) and (9) with $\alpha = 1/\pi\varepsilon\lambda z$.

In theory, PAD-MBA does not require an intermediate phase-retrieval step since it implements both the phase retrieval and the tomographic reconstruction in a single formula. However, this is difficult to fulfill in computer programs because it requires very large amounts of RAM. In *PITRE*, PAD-MBA is separated into two steps: firstly, filtering $g_\theta(x,y)$ with the filter in (9), and then applying the back-projection to obtain the reconstruction results.

2.3. DEI information extraction

DEI is an X-ray imaging modality using monochromatic X-rays from a synchrotron radiation facility. It utilizes an analyser crystal placed between the sample and the detector. This analyser acts as an angular band-pass filter: the acceptance is determined by the full width at half-maximum $\Delta\theta_D$ of the rocking curve $R(\theta)$, and it is commensurate with the tiny angular displacements that arise when X-ray photons are deviated from their initial path crossing the sample (Chapman *et al.*, 1997). Therefore, sample absorption, refraction and ultra-small-angle scattering (USAXS) information are recorded on the detector. Separating this information can be carried out by using DEI extraction algorithms, which typically require a few DEI images collected at different positions of $R(\theta)$. In *PITRE*, the conventional DEI (CDEI) (Chapman *et al.*, 1997) and generalized DEI (GDEI) (Rigon *et al.*, 2007a,b; Chou *et al.*, 2007) algorithms are implemented. In the following, the principle of both algorithms will be briefly presented.

For convenience, let us denote R_i, $\dot{R}_i$ and $\ddot{R}_i$, respectively, as the $R(\theta)$ and its first and second derivative values calculated in the angular position θ_i ($i = [1,3]$), with $i = 1, 2$ and 3 representing the low

half-slope (on the left of the peak position), peak and high half-slope of $R(\theta)$, respectively. $I(\theta_i)$ are the recorded images for the respective angular position θ_i. I_R is the apparent absorption intensity, $\Delta\theta_R$ and $\Delta\theta_S$ are refraction and scattering angles, respectively, for photons leaving the object plane (Rigon *et al.*, 2007b).

2.3.1. Conventional DEI algorithm. The CDEI algorithm combines two half-slope images $I(\theta_i)$ ($i = 1, 3$) to extract a couple of new images: the apparent absorption image, which is similar to the conventional absorption image but also includes extinction contrast (*i.e.* contrast generated by the rejection of small-angle scattering), and the refraction image, which represents the distribution of the refraction angle at each point in the object plane. According to the first-order Taylor approximation of $R(\theta)$, the intensity $I(\theta_i)$ ($i = 1, 3$) can be expressed as follows (Chapman *et al.*, 1997),

$$I(\theta_i) = I_R\left[R_i + \dot{R}_i\Delta\theta_R\right] \qquad (i = 1, 3). \qquad (10)$$

By solving these two equations, the apparent absorption I_R and the refraction image $\Delta\theta_R$ can be extracted as in the following equations (Chapman *et al.*, 1997),

$$\begin{aligned} I_R &= \frac{I_3\dot{R}_1 - I_1\dot{R}_3}{R_3\dot{R}_1 - R_1\dot{R}_3}, \\ \Delta\theta_R &= \frac{I_1 R_3 - I_3 R_1}{I_3\dot{R}_1 - I_1\dot{R}_3}. \end{aligned} \qquad (11)$$

The CDEI-CT slice can be reconstructed by applying the standard FBP algorithm to I_R and $\Delta\theta_R$ (Dilmanian *et al.*, 2000).

2.3.2. Generalized DEI algorithm. The CDEI algorithm does not take USAXS into account. In general a sample may produce a combination of absorption, refraction and scattering effects. Considering all these signals, the GDEI algorithm provides a simple way to obtain absorption, refraction and USAXS information by utilizing three DEI images, $I(\theta_i)$, $i = [1,3]$ (Rigon *et al.*, 2007a; Chou *et al.*, 2007). Considering the scattering in DEI and utilizing the second-order Taylor approximation, the intensity $I(\theta_i)$, $i = [1,3]$, can be obtained as follows (Rigon *et al.*, 2007b),

$$I(\theta_i) = I_R\left[R_i + \dot{R}_i\Delta\theta_R + \frac{1}{2}\ddot{R}_i(\Delta\theta_R)^2 + \frac{1}{2}\ddot{R}_i\sigma_{\Delta\theta}^2\right], \quad i = [1,3], \quad (12)$$

where $\sigma_{\Delta\theta_S}^2$ is the variance of the USAXS distribution (Rigon *et al.*, 2007b). The solution of the system in (12) provides three parametric images, namely the apparent absorption image I_R, the refraction image $\Delta\theta_R$ and the USAXS image $\sigma_{\Delta\theta_S}^2$. A straightforward calculation gives the results reported in the following equations (Rigon *et al.*, 2007b),

$$\begin{aligned} I_R &= \sum_{ijk}\varepsilon_{ijk}I_i\dot{R}_j\ddot{R}_k \Big/ \sum_{ijk}\varepsilon_{ijk}R_i\ddot{R}_j\ddot{R}_k, \\ \Delta\theta_R &= -\sum_{ijk}\varepsilon_{ijk}I_i R_j\ddot{R}_k \Big/ \sum_{ijk}\varepsilon_{ijk}I_i\dot{R}_j\ddot{R}_k, \\ \sigma_{\Delta\theta_S}^2 &= 2\sum_{ijk}\varepsilon_{ijk}I_i R_j\dot{R}_k \Big/ \sum_{ijk}\varepsilon_{ijk}I_i\dot{R}_j\ddot{R}_k - (\Delta\theta_R)^2, \end{aligned} \qquad (13)$$

where ε_{ijk} is the totally anti-symmetric tensor. As in CDEI, the 3D information of I_R, $\Delta\theta_R$ and $\sigma_{\Delta\theta_S}^2$ can be reconstructed by applying the standard FBP algorithm (Rigon *et al.*, 2008).

2.4. Sinogram generation

In parallel-beam CT, the sinogram represents the signal measured along a given detector row in the imaging plane for all CT scan angles. In *PITRE*, this is an intermediate step of slice reconstruction from projections. The sinogram generation method in *PITRE* is as follows.

computer programs

Firstly, *PITRE* allocates a series of empty sinograms, whose size corresponds to the projection size and number of CT projections, in the computer memory. Thereby *PITRE* utilizes the IDL allocated physical memory size (IDL-APMS) that is provided by the user in the *PITRE* panel. The IDL-APMS is relative to the operation system (OS)-free-PMS. Designed by IDL, it is smaller than the OS-free-PMS in order to guarantee that the OS runs smoothly. In case the provided size is larger than the IDL-APMS, *PITRE* returns an error. Secondly, *PITRE* loads the projections in sequence, accomplishes the flat-field and dark-field correction, and fills the empty sinograms accordingly. Finally, *PITRE* saves the sinograms to the hard disk in 32-bit single-precision float TIFF format. If the IDL-APMS cannot hold all sinograms at a time, *PITRE* will automatically divide the sinogram creation into multiple runs, determined by the IDL-APMS and the total sinogram size.

2.5. Sinogram pre-processing before reconstruction

Pre-processing the sinogram before reconstruction is required since the collected CT data are often quite far from the ideal case. *PITRE* provides normalization, image cropping, extended-view CT data handling, ring artifacts removal, and rotation center determination. Moreover, the natural logarithm and filtering are applied to absorption CT data according to the theory. All these pre-processing features will be explained in the following.

The normalization can be used to correct some beam variations during the CT data collection. In SR-CT the X-ray beam delivered from the SR source is very intense. Owing to thermal fluctuations in the cooling system of the monochromator, the intensity may change during data acquisition. In addition, time-dependent instabilities of the image receptor cannot be excluded. Moreover, the current in the storage ring of the SR facility could change with time and so will the flux reaching the detector. Thus, a normalization procedure is needed, which will equalize the intensity of projections collected at different times, provided the intensity variations are sufficiently homogeneous. The procedure is: firstly, select some columns in the background of the sinogram, *i.e.* which do not contain the sample; secondly, obtain the mean value of the selected columns for each row; finally, divide all pixels in each row by this mean value.

Image cropping is used to crop the unwanted space in the sinogram. It is well known that the reconstruction time is proportional to the size of the sinogram and slice. Usually the sinogram possesses unwanted background on the left- or right-hand side. *PITRE* allows the user to crop these backgrounds out in order to speed up the reconstruction. Moreover, *PITRE* also allows the sinogram to be cropped in the vertical direction to get rid of unwanted or redundant projections that are rows in the top or bottom of the sinogram. This will be useful for instance in continuous CT scans, which typically cover more than the required angular range, or when the detector keeps acquiring projections before and after the actual CT scanning. The user can interactively refine the vertical cropping values by checking the corresponding result image.

The extended-view CT data handling deals with parallel CT data collected in the $[0, 2\pi)$ range in order to artificially extend the field of view (FOV) of the CT system (Haberthur *et al.*, 2010). The FOV in SR-CT is a problematic issue especially with a high-resolution detector. For parallel-beam CT, data are typically collected in the $[0, \pi)$ angular range and this is sufficient for reconstruction, since the $[\pi, 2\pi)$ projections are symmetrical with the $[0, \pi)$ ones. Owing to this symmetry, it is possible to almost double the FOV by using $[0, 2\pi)$ CT scan data. In more detail, if the sample size is larger than but less than two times the FOV, then a complete CT data set cannot be collected

with a $[0, \pi)$ scan. However, by placing the rotation axis near one edge of the FOV and by using the symmetry between the $[0, \pi)$ and $[\pi, 2\pi)$ scans, one complete sinogram can be obtained, as if the complete sample fits the FOV in a $[0, \pi)$ data collection. Extended-view CT data handling converts the $[0, 2\pi)$ raw scan data into one complete $[0, \pi)$ sinogram. It should be noted that it is an optional pre-processing tool that is used only for this specific CT data type. In *PITRE*, the overlap range determination between the $[0, \pi)$ and $[\pi, 2\pi)$ scan mode is not automatic; instead it requires the user to manually refine this by verifying the resulting slices. This works well as long as the rotation axis is within the FOV.

Ring artifacts are common features in CT imaging and are due, for instance, to drifts in the detector element sensitivity, non-linear detector element response and higher-energy harmonics in the incident beam. These defects will cause vertical stripes to be observed in the sinogram. As a result, after back-projection, the ring artifacts will superimpose on the CT slices. Reducing them is possible by using flat-field correction, but it is unlikely to completely remove them. Thus a specific procedure is needed (Munch *et al.*, 2009). *PITRE* provides a simple ring artifacts removal method. The procedure is: firstly, compute the average row of the sinogram by summing down each column and dividing by the number of rows. This average row should have very little high-frequency content, since real objects will be blurred out when computing the average row; secondly, compute the magnitude of these detector anomalies by subtracting a smoothed version of the average row; finally, subtract the result of the previous step, the detector anomalies, from each row in the sinogram. This result presents much less vertical striping. As mentioned above, ring artifacts on the slice are strictly related to vertical stripes on the sinogram, and thus this procedure will reduce them.

The rotation center determination locates the CT rotation axis in the sinogram center. The CT reconstruction algorithm, by default, assumes that the rotation axis is in the center of the sinogram, which is difficult to accomplish in the practical case. Therefore, the rotation center determination is an essential pre-processing step. The method is to shift the sinogram horizontally by the difference between the image center and the position of the rotation axis. *PITRE* will provide an estimation value of the position of the rotation axis by calculating the center of gravity of the sinogram for each row and a subsequent curve fitting with a sine wavefunction. The user can further refine the rotation center manually by verifying the resulting slices. When the CT scan system shows some misalignment, the rotation axis could be tilted with respect to the vertical axis of the detector and in theory the collected CT data are no longer correct. In the case that the misalignment is small, a reasonable reconstruction result can still be obtained by adjusting the rotation center values on a slice-per-slice basis. In this case the rotation center is different for each sinogram. *PITRE* provides an option to dynamically adjust it; the procedure is: once the rotation center for the first and the last sinogram have been determined manually, then *PITRE* will use a linear interpolation between these two values for the others, taking into account that the rotation center values are an arithmetic progression in this case.

Before applying FBP, and in the case of conventional absorption CT data, the natural logarithm is applied to the sinograms. However, it should be noted that this procedure would not be applied to sinograms of phase retrieval and to refraction and the USAXS extracted from DEI, as demonstrated in equations (4), (7), (10) and (12). Moreover, for the PAD-MBA calculation, filtering is already applied during phase retrieval using the $|\xi|$ parameter in (9) (Bronnikov, 2002). *PITRE* will therefore automatically enable or disable the natural logarithm and filtering functions according to the data type.

In brief, the sinogram pre-processing procedure can be summarized in the following virtual equation,

$$\text{sinogram}_{\text{processed}} = (filtering)\{ln[(normalization)^{\text{op}}\\ (cropping)(extended\ view)^{\text{op}}(ring)^{\text{op}}\\ (shifting)\text{sinogram}]\}, \quad (14)$$

where (*italic*) means a processing function, while the superscript 'op' denotes an optional function that can be enabled or disabled by the user.

2.6. Slice reconstruction

Two reconstruction algorithms, FBP (Kak & Slaney, 2001) and Gridrec (Dowd *et al.*, 1999), which is a FFT-based reconstruction algorithm, are provided in *PITRE*. FBP is the most common algorithm used in the tomographic reconstruction. The Gridrec algorithm is from Brookhaven and was later modified to be called from IDL by Mark Rivers (Rivers *et al.*, 2004; GSECARS, 2012). According to Dowd's experience, the Gridrec algorithm has reduced the reconstruction times for $650 \times 650 \times 515$ datasets from several hours to less than ten minutes compared with the FBP algorithm (Dowd *et al.*, 1999). The performance and reconstruction accuracy of Gridrec was further investigated by Marone *et al.* (2010). In *PITRE* the user can easily change between these two algorithms *via* a combo-box-based option.

3. Implementation

Present-day PCs can run *PITRE* without any problem. One suggestion is to install a large RAM size owing to the sinogram generation method as mentioned in §2.4. Moreover, it is recommended to use a 64-bit version operation system with *PITRE* rather than a 32-bit version in case the PC RAM size is larger than 4 Gbyte.

3.1. Configuration

The configuration for running the software is as follows:

(i) Install 32/64-bit IDL (version 7.1 or higher), which can be downloaded from the EXELIS website (IDL, 2012) after a simple registration, on windows XP (or a newer version). The IDL Virtual Machine is included in the IDL installation file and does not require a license to run.

(ii) Download the *PITRE* installer (32/64-bit) (PITRE, 2012) and run it as Administrator.

(iii) Reboot the computer.

(iv) Use IDL Virtual Machine to open 'PITRE.sav' to run the software.

The installer will add 'C:\PITRE\lib\', which includes external libraries for *PITRE*, to the system environment variable 'Path'. In this way, *PITRE* will automatically locate and call the external libraries, such as Gridrec (Dowd *et al.*, 1999; GSECARS, 2012) and GraphicsMagick (GraphicsMagick, 2012). All the required external libraries for *PITRE* are included in the installer and will be installed automatically.

3.2. Supported data types

As input, *PITRE* accepts TIFF (tagged image file format, 8-bit unsigned integer, 16-bit unsigned integer and 32-bit single-precision float format), PNG (8-bit unsigned integer) and BMP (8-bit unsigned integer) format images. The output is a dataset of 32-bit single-precision float TIFF images. Moreover, *PITRE* provides a solution for converting a 12-bit unsigned integer TIFF (compressed or uncompressed) into a 16-bit unsigned integer TIFF by using GraphicsMagick as a plug-in (GraphicsMagick, 2012). *PITRE* also provides specific features to elaborate data acquired by the PICASSO detector (Rigon *et al.*, 2010a; Lopez *et al.*, 2011).

The name of projection, flat-field and dark-field images is a combination of a prefix and index number. The prefix of a projection, flat field and dark field must be 'tomo_', 'flat_' and 'dark_', respectively. All projection, flat-field and dark-field images must be named progressively, and saved in the same folder. In order to meet the alphabetical sorting rule in IDL, the digit number of all image index numbers must be the same. One can accomplish this by adding zero(s) to the small index numbers.

During the flat-field and dark-field correction, in order to minimize the statistical noise introduced by the correction it is preferable to take a series of flat-field and dark-field images and average them before using them to correct the projections. *PITRE* automatically processes series of flat-field and dark-field images to obtain the average result. In the case where flat-field images have been acquired not only at the beginning and the end but also during a CT scan, *PITRE* needs input information about the number of flat-field images and projections that are collected for each interval, and will then process them automatically.

4. Graphical user interface (GUI)

In this section, the GUIs of *PITRE* (PPCI Tab and ProjSino Tab) and *PITRE_BM* will be shown.

4.1. The GUI of *PITRE*

As shown in Fig. 2, the GUI of *PITRE* is subdivided into five tab panels that correspond to PPCI, DEI, SinoConvert, ProjSino and Slice. These subpanels are accommodated in one global panel or base, which is effective for all tab panels. Each tab is associated with a specific task: the PPCI tab handles phase retrieval of PPCT projections; the DEI tab extracts apparent absorption, refraction and scattering from DEI-CT projections; the SinoConvert tab converts the PICASSO-CT data into a readable image format; the ProjSino tab processes sinogram creation, sinogram pre-processing and slice reconstruction; the Slice tab is used to display the reconstructed slice and corresponding reconstruction parameters.

Fig. 2 shows the PPCI tab panel displaying a projection image of an ant after flat-field and dark-field correction. The three drop-down menus located on the menu bar of the GUI allow images to be loaded for each tab or to convert images. The first row of the *PITRE* GUI is a global panel that is effective for all the tab panels. It includes the flat-field and dark-field correction method, a processing status indicator, and so on. As depicted in Fig. 2, after loading the PPCT projection the full path and size of the projection and number of projection in the same directory will be provided in the panel. *PITRE* can load multi-SDD (maximum 5) PPCT data by changing the 'SDD index' in the panel before loading the PPCT projection in the menu 'Load image'. Moreover, the PPCI phase-retrieval algorithm, padding, PPCT parameters and button for triggering the phase retrieval are also provided in the panel. The reason for implementing the padding is due to the FFT used during the phase retrieval that requires the size of the projection image to be an integer power of two and to increase the spatial frequency sampling. The loaded image is shown in the visualizing panel on the right. The image is viewed with its original size scale (in pixels) in both directions. However, the image may have been rescaled in order to fit the panel, but its aspect ratio is preserved. After choosing the phase-retrieval algorithms and

entering the PPCT parameters, phase retrieval can be launched by clicking the 'Single' or 'All' button for phase retrieval of single or all projections, respectively. Clicking the 'Task' button will save this phase-retrieval task, which will be handled by *PITRE_BM*, as a text file on the hard disk in the default directory 'C:\PITRE\TaskToGo\'.

The result of the PPCI tab panel will appear in the ProjSino tab panel, as shown in Fig. 3. The first row of this tab contains a radio button, which is used for switching between Projection images (base) and Sinogram images (Base). It also contains a CT data source indicator 'Source(Proj-Sino)', which will be automatically set to the phase-retrieval algorithm, DEI extraction information or 'raw' value. Based on the 'Source' information, *PITRE* will process the CT data set accordingly. The ProjSino tab has two independent functional bases, the Projection base and the Sinogram base. The projection base handles the sinogram generation while the sinogram base assesses the sinogram pre-processing and reconstruction. In the projection base the user can generate a single, a subset or an entire set of sinograms predefined by the 'SinoSN(B-E)' values. The 'IDL-APMS' option is the IDL-APMS value which has been introduced in §2.4. The sinogram base contains all the sinogram pre-processing functions and parameters (§2.5). Editing of the pre-processing parameters will be automatically enabled or disabled according to the specific pre-processing function. As depicted in Fig. 3, three different kinds of tasks (as indicated in the task button) can be created in this tab for the *PITRE_BM*. The reconstructed slice and the reconstruction parameters will be shown on the Slice tab.

4.2. The GUI of *PITRE_BM*

PITRE handles one task at a time. Typically, in one SR-CT beam time a lot of CT data will be collected, *i.e.* meaning many data processing tasks for *PITRE*. Users may open several *PITRE* for multi-task processing, but this will slow down the processing speed for a single task and finally will increase the overall data throughput. *PITRE_BM* is a batch processing manager for *PITRE*. It executes a series of tasks ('jobs'), which is created *via PITRE*, without manual intervention. The *PITRE_BM* GUI is presented in Fig. 4, in which a 'Projection2Slice' task is running. By default, all tasks created by *PITRE* will be saved as a text file in the default directory 'C:\PITRE\TaskToGo\', and they will be moved to the default directory 'C:\PITRE\TaskFinished\' once finished. The *PITRE_BM* GUI is very simple because it just executes a task file which is generated by *PITRE* and contains all support parameters. *PITRE_BM* provides the file name and task type of the current task, the remaining number of tasks in the 'C:\PITRE\TaskToGo\' directory, the 'IDL-APMS' option, the processing status indicator and an image viewer for verifying the current task result. The task list is loaded into the GUI by clicking the 'Load' button. The 'GO!!' button launches the processing until all tasks are finished. When *PITRE_BM* is running, new tasks can be added onto the stack. *PITRE_BM* will refresh the task list once it finishes the current one. In the absence of new tasks on the stack, the program can be launched manually to start a new batch processing.

Figure 2
GUI of *PITRE*: the PPCI tab panel is selected.

Figure 3
GUI of *PITRE*: the ProjSino tab panel is selected.

5. Examples

Depicted in Figs. 5(*a*), 5(*b*) and 5(*c*) are DEI projections at the low half-slope, the peak and the high half-slope, respectively, of the analyser rocking curve of a custom-made phantom that simulates the three physical effects. Shown in Figs. 5(*d*)–5(*f*) are the apparent absorption, refraction and USAXS information extracted from Figs. 5(*a*)–5(*c*) using the GDEI algorithm. The phantom consists of a Plexiglas cylinder, 15 mm in diameter, in which four holes have been drilled under different angles ranging from
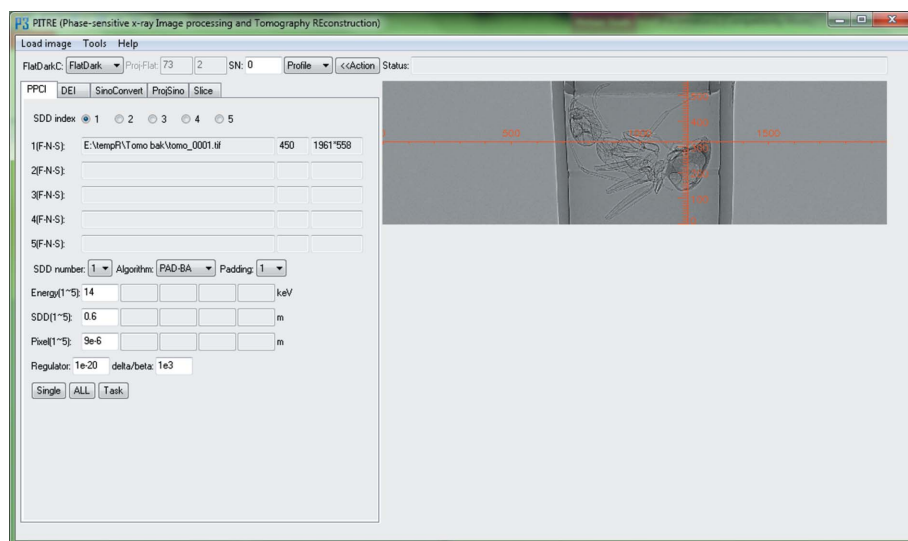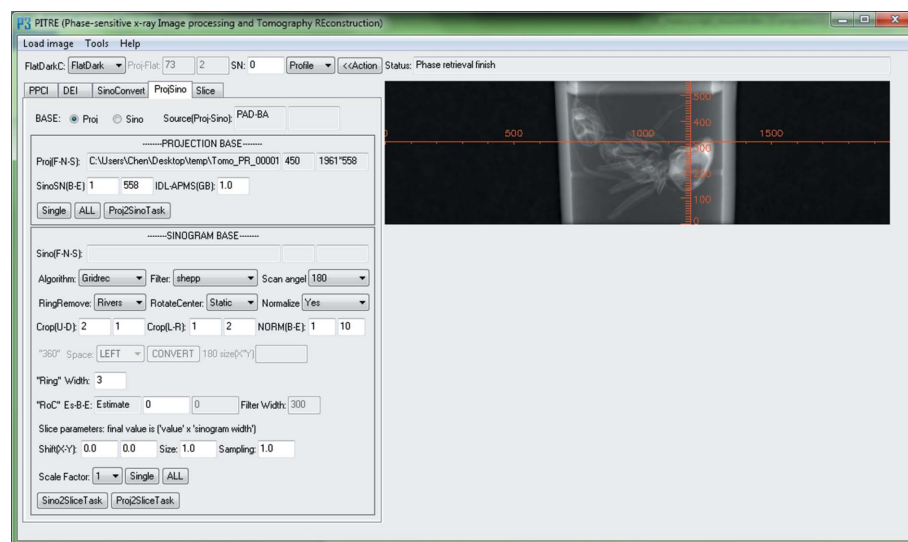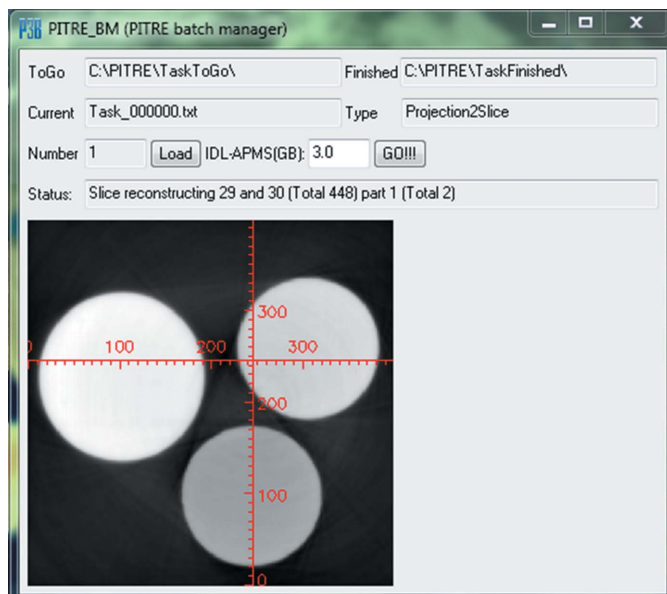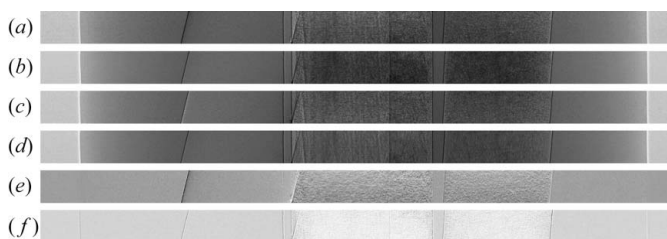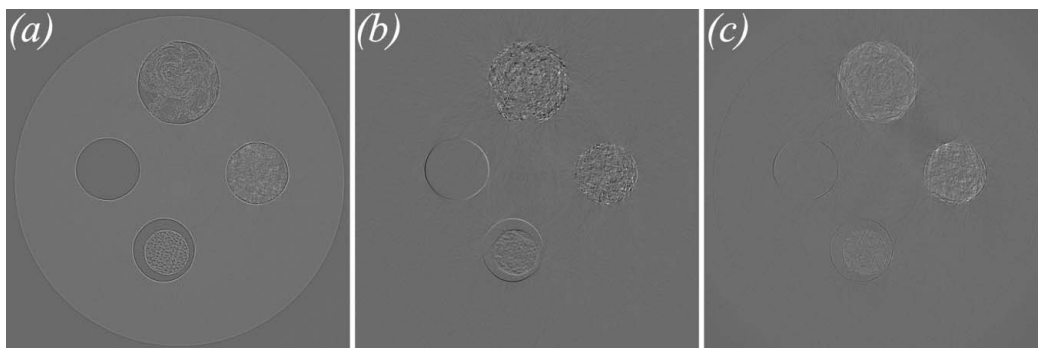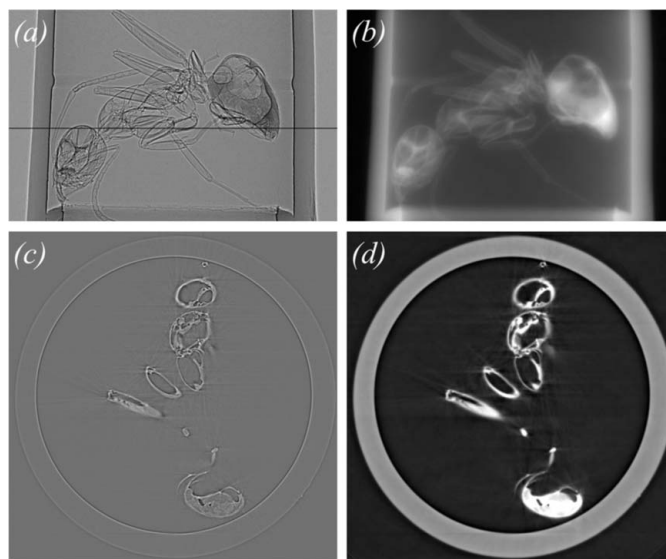
Figure 4
GUI of *PITRE_BM*.

Figure 5
DEI projections and their extracted information. (*a*), (*b*) and (*c*) are DEI projections at the same rotation angle of low half-slope, peak and high half-slope of the rocking curve, respectively; (*d*), (*e*) and (*f*) are the apparent absorption, refraction and USAXS information extracted from (*a*)–(*c*) using the GDEI algorithm.

0° (*i.e.* parallel) to 15° with respect to the cylinder axis. Three of the four holes are filled with soft paper, PMMA microspheres and a toothpick, while the 15° hole is left empty. In this case, different vertical gradients of the refractive index are obtained by the inclination of the holes, and different amounts of absorptive, refractive and scattering features are introduced by the paper, the microspheres and the wooden sample (Rigon *et al.*, 2008). As shown in Fig. 5, the apparent absorption image (Fig. 5*d*) is similar to the DEI projection

Figure 6
DEI-CT reconstruction results: (*a*), (*b*) and (*c*) are the absorption, refraction and USAXS slices, respectively.
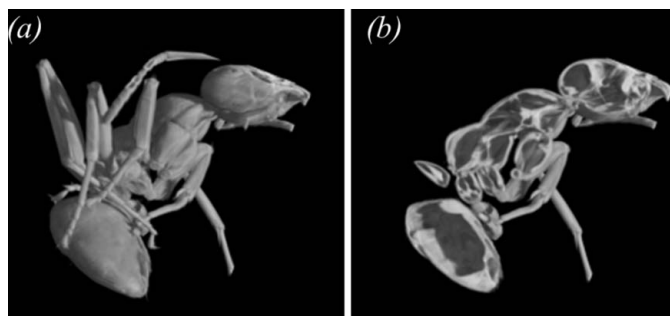

Figure 7
PPCT data and processed result of an ant sample. PPCT projection without (*a*) and with (*b*) phase retrieval using the PAD-BA algorithm; reconstructed slice without (*c*) and with (*d*) phase retrieval at the line position of (*a*).

at the rocking-curve peak position (Fig. 5*b*), which in turn is similar to the conventional CT projection. Different vertical gradients of the refractive index of the holes are prominent in the refraction image in Fig. 5(*e*). The inclined holes give rise to black and white shades, while the vertical Plexiglas cylinder possesses no refractive signal. In the USAXS image (Fig. 5*f*) the paper and the microspheres yield a bright signal. Both materials introduce strong scattering owing to multiple refraction in arbitrary directions due to their randomly oriented fine structures. Fig. 6 shows DEI-CT reconstruction results, in which Figs. 6(*a*), 6(*b*) and 6(*c*) are the absorption, refraction and USAXS slices, respectively.

Fig. 7 shows PPCT data and the processed result of a biological sample, in this case an ant. Figs. 7(*a*) and 7(*b*) show a PPCT projection without and with phase retrieval, respectively, using the PAD-BA algorithm, while Figs. 7(*c*) and 7(*d*) are reconstructed slices at the line position indicated in Fig. 7(*a*), again without and with phase retrieval. For convenience the ant sample was put into a plastic tube (diameter ∼5 mm) during PPCT data acquisition; 900 PPCT equiangular projections were collected within an angular range of 180°. As Fig. 7(*c*) shows, the sample outline is very clear since there is strong edge enhancement, but the contrast difference between the plastic and the ant is difficult to distinguish, while in the phase-retrieval image (Fig. 7*d*) there is obviously a contrast difference between the plastic and the ant, and the outline of the sample is clearly reconstructed too. Fig. 8 shows 3D rendering images of the ant sample after applying the PAD-BA. The details of the ant, such as the legs and antennae, are well visualized in the figures. By virtually cutting the sample it is also possible to visualize the internal details of the ant (Fig. 8*b*).

Figure 8
Volume renderings of the ant sample after applying the PAD-BA. In (a) the whole ant is visible, while in (b) a virtual cut of the sample is shown. The volume renderings have been obtained by using the commercial software *VGStudio MAX 2.0* (VGStudio Max, 2012).

6. Conclusions

We have presented the *PITRE* software that allows phase-sensitive X-ray image processing and tomography reconstruction. *PITRE* supports phase retrieval for PPCT, DEI information extraction and parallel-beam tomography reconstruction for conventional absorption CT data and for PPCT phase retrieved and DEI-CT extracted information; it provides useful sinogram pre-processing functions. *PITRE_BM* is a comprehensively supplemented batch processing manager for *PITRE*. It executes a series of tasks ('jobs'), which is created *via PITRE*, without manual intervention. *PITRE* is freeware, independent, user-friendly and robust software, which might be a versatile tool for SR-CT applications. The software can be obtained from http://webint.ts.infn.it/en/research/exp/beats2/pitre.html or https://sites.google.com/site/rongchangchen/pitre-download.

References

Abrami, A. *et al.* (2004). *Nucl. Instrum. Methods Phys. Res. A*, **548**, 221–227.
Arhatari, B. D., De Carlo, F. & Peele, A. G. (2007). *Rev. Sci. Instrum.* **78**, 053701.
Bonse, U. (2008). *Proc. SPIE*, **7078**, 707802.
Born, M. & Wolf, E. (1999). *Principles of Optics*, 7th ed. Cambridge University Press.
Bronnikov, A. V. (2002). *J. Opt. Soc. Am. A*, **19**, 472–480.
Brun, F., Mancini, L., Kasae, P., Favretto, S., Dreossi, D. & Tromba, G. (2010). *Nucl. Instrum. Methods Phys. Res. A*, **615**, 326–332.
Chapman, D., Thomlinson, W., Johnston, R. E., Washburn, D., Pisano, E., Gmur, N., Zhong, Z., Menk, R., Arfelli, F. & Sayers, D. (1997). *Phys. Med. Biol.* **42**, 2015–2025.
Chen, R. C., Longo, R., Rigon, L., Zanconati, F., De Pellegrin, A., Arfelli, F., Dreossi, D., Menk, R.-H., Vallazza, E., Xiao, T. Q. & Castelli, E. (2010). *Phys. Med. Biol.* **55**, 4993–5005.
Chen, R. C., Rigon, L. & Longo, R. (2011a). *J. Phys. D*, **44**, 495401.
Chen, R. C., Xie, H. L., Rigon, L., Longo, R., Castelli, E. & Xiao, T. Q. (2011b). *Opt. Lett.* **36**, 1719–1721.
Chou, C. Y., Anastasio, M. A., Brankov, J. G., Wernick, M. N., Brey, E. M., Connor, D. M. & Zhong, Z. (2007). *Phys. Med. Biol.* **52**, 1923–1945.
Cloetens, P., Barrett, R., Baruchel, J., Guigay, J. P. & Schlenker, M. (1996). *J. Phys. D*, **29**, 133–146.
Cloetens, P., Ludwig, W., Baruchel, J., Van Dyck, D., Van Landuyt, J., Guigay, J. P. & Schlenker, M. (1999). *Appl. Phys. Lett.* **75**, 2912–2914.
Cloetens, P., Pateyron-Salomé, M., Buffière, J. Y., Peix, G., Baruchel, J., Peyrin, F. & Schlenker, M. (1997). *J. Appl. Phys.* **81**, 5878–5886.
CXRO (2012). *CXRO*, http://henke.lbl.gov/optical_constants/getdb2.html.
Deng, B., Yang, Q., Xie, H. L., Du, G. H. & Xiao, T. Q. (2011). *Chin. Phys. C*, **35**, 402–404.
Dilmanian, F. A., Zhong, Z., Ren, B., Wu, X. Y., Chapman, L. D., Orion, I. & Thomlinson, W. C. (2000). *Phys. Med. Biol.* **45**, 933–946.
Dowd, B. A., Campbell, G. H., Marr, R. B., Nagarkar, V., Tipnis, S., Axe, L. & Siddons, D. P. (1999). *Proc. SPIE*, **3772**, 224–326.
Fife, J. L., Rappaz, M., Pistone, M., Celcer, T., Mikuljan, G. & Stampanoni, M. (2012). *J. Synchrotron Rad.* **19**, 352–358.
Fitzgerald, R. (2000). *Phys. Today*, **53**, 23–26.
GraphicsMagick (2012). *GraphicsMagick*, http://www.graphicsmagick.org/index.html.
Groso, A., Abela, R. & Stampanoni, M. (2006). *Opt. Express*, **14**, 8103–8110.
GSECARS (2012). *GSECARS*, http://cars9.uchicago.edu/software/idl/tomography.html.
Guigay, J. P. (1977). *Optik*, **49**, 121–125.
Gureyev, T. E., Davis, T. J., Pogany, A., Mayo, S. C. & Wilkins, S. W. (2004). *Appl. Opt.* **43**, 2418–2430.
Gureyev, T. E., Nesterets, Y., Ternovski, D., Thompson, D., Wilkins, S. W., Stevenson, A. W., Sakellariou, A. & Taylor, J. A. (2011). *Proc. SPIE*, **8141**, 81410B.
Gureyev, T. E., Paganin, D. M., Myers, G. R., Nesterets, Y. I. & Wilkins, S. W. (2006). *Appl. Phys. Lett.* **89**, 034102.
Haberthür, D., Hintermüller, C., Marone, F., Schittny, J. C. & Stampanoni, M. (2010). *J. Synchrotron Rad.* **17**, 590–599.
Henke, B. L., Gullikson, E. M. & Davis, J. C. (1993). *Atom. Data. Nucl. Data Tables*, **54**, 181–342.
Hintermüller, C., Marone, F., Isenegger, A. & Stampanoni, M. (2010). *J. Synchrotron Rad.* **17**, 550–559.
Holotomography (2012). *Holotomography*, http://www.esrf.eu/UsersAndScience/Publications/Highlights/1999/Tech-Inst/holotom.html.
Hu, J. Z., Wu, T. D., Zeng, L., Liu, H. Q., He, Y., Du, G. H. & Lu, H. B. (2012). *Phys. Med. Biol.* **57**, N55–N63.
IDL (2012). *IDL*, http://www.exelisvis.com/language/en-us/productsservices/idl.aspx.
ImageJ (2012). *ImageJ*, http://rsbweb.nih.gov/ij/.
Kak, A. C. & Slaney, M. (2001). *Principles of Computerized Tomographic Imaging*. Philadelphia: Society of Industrial and Applied Mathematics.
Liu, X. X., Zhao, J., Sun, J. Q., Gu, X., Xiao, T. Q., Liu, P. & Xu, L. X. (2010). *Phys. Med. Biol.* **55**, 2399–2409.
Lopez, F. C., Rigon, L., Longo, R., Arfelli, F., Bergamaschi, A., Chen, R. C., Dreossi, D., Schmitt, B., Vallazza, E. & Castelli, E. (2011). *J. Instrum.* **6**, C12031.
Lu, W., Dong, Z., Liu, Z., Fu, W., Peng, Y., Chen, S., Xiao, T., Xie, H., Du, G., Deng, B. & Zhang, X. (2010). *J. Surg. Res.* **164**, E193–E199.
Marone, F., Munch, B. & Stampanoni, M. (2010). *Proc. SPIE*, **7804**, 780410.
Momose, A. (2005). *Jpn. J. Appl. Phys.* **44**, 6355–6367.
Montanari, F., Mancini, L. & Dreossi, D. (2003). *SYRMEP_Tomo_Project tutorial: Internet Report*, Sincrotrone Trieste, Italy (http://www.ts.infn.it/physics/experiments/syrma/SYRMEP/Tutorial_tomo_program.ppt).
Munch, B., Trtik, P., Marone, F. & Stampanoni, M. (2009). *Opt. Express*, **17**, 8567–8591.
Nugent, K. A., Gureyev, T. E., Cookson, D. F., Paganin, D. & Barnea, Z. (1996). *Phys. Rev. Lett.* **77**, 2961–2964.
Paganin, D., Mayo, S. C., Gureyev, T. E., Miller, P. R. & Wilkins, S. W. (2002). *J. Microsc.* **206**, 33–40.
Pani, S., Longo, R., Dreossi, D., Montanari, F., Olivo, A., Arfelli, F., Bergamaschi, A., Poropat, P., Rigon, L., Zanconati, F., Dalla Palma, L. & Castelli, E. (2004). *Phys. Med. Biol.* **49**, 1739–1754.
PITRE (2012). *PITRE*, http://webint.ts.infn.it/en/research/exp/beats2/pitre.html or https://sites.google.com/site/rongchangchen/pitre-download.
Rigon, L., Arfelli, F., Bergamaschi, A., Chen, R. C., Dreossi, D., Longo, R., Menk, R. H., Schmitt, B., Vallazza, E. & Castelli, E. (2010a). *Nucl. Instrum. Methods Phys. Res. A*, **617**, 244–245.
Rigon, L., Arfelli, F. & Menk, R. H. (2007a). *J. Phys. D*, **40**, 3077–3089.
Rigon, L., Arfelli, F. & Menk, R. H. (2007b). *Appl. Phys. Lett.* **90**, 114102.
Rigon, L., Astolfo, A., Arfelli, F. & Menk, R. H. (2008). *Eur. J. Radiol.* **68**, S3–S7.
Rigon, L. *et al.* (2010b). *E-Preserv. Sci.* **7**, 71–77.
Rigon, L., Tapete, F., Dreossi, D., Arfelli, F., Bergamaschi, A., Chen, R.-C., Longo, R., Menk, R.-H., Schmitt, B., Vallazza, E. & Castelli, E. (2011). *Nucl. Instrum. Methods Phys. Res. A*, **628**, 419–422.
Rivers, M. L., Wang, Y. & Uchida, T. (2004). *Proc. SPIE*, **5535**, 783–791.

Snigirev, A., Snigireva, I., Kohn, V., Kuznetsov, S. & Schelokov, I. (1995). *Rev. Sci. Instrum.* **66**, 5486–5492.

Sodini, N., Dreossi, D., Chen, R. C., Fioravanti, M., Giordano, A., Herrestal, P., Rigon, L. & Zanini, F. (2012). *J. Cult. Herit.* In the press.

Tang, R. B., Xi, Y., Chai, W. M., Wang, Y. T., Guan, Y. J., Yang, G. Y., Xie, H. L. & Chen, K. M. (2011). *Phys. Med. Biol.* **56**, 3503–3512.

VGStudio Max (2012). *VGStudio Max*, http://www.volumegraphics.com/en/products/vgstudio-max.html.

Weitkamp, T., Haas, D., Wegrzynek, D. & Rack, A. (2011). *J. Synchrotron Rad.* **18**, 617–629.

Wilkins, S. W., Gureyev, T. E., Gao, D., Pogany, A. & Stevenson, A. W. (1996). *Nature (London)*, **384**, 335–338.

Wu, X. Z., Liu, H. & Yan, A. M. (2005). *Opt. Lett.* **30**, 379–381.

X-TRACT (2012). *X-TRACT*, http://www.ts-imaging.net/Services/AppInfo/X-TRACT.aspx.

Yang, Q., Deng, B., Lv, W., Shen, F., Chen, R., Wang, Y., Du, G., Yan, F., Xiao, T. & Xu, H. (2012). *J. Synchrotron Rad.* **19**, 210–215.

Zhang, X. Y., Zhang, D. M., Yan, X. H., Liu, C. L., Dang, R. S., Xiao, T. Q. & Zhu, P. P. (2011). *Anal. Bioanal. Chem.* **401**, 803–808.